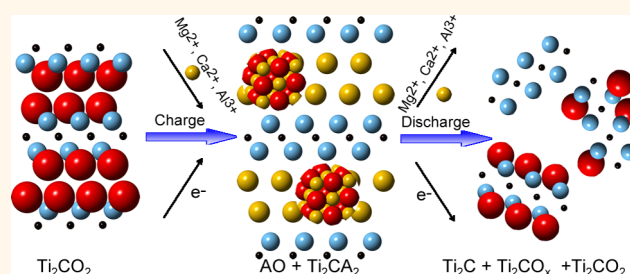


Prediction and Characterization of MXene Nanosheet Anodes for Non-Lithium-Ion Batteries

Yu Xie,^{†,*} Yohan Dall'Agnese,^{‡,§} Michael Naguib,^{§,||} Yury Gogotsi,^{§,*} Michel W. Barsoum,[§] Houlong L. Zhuang,[†] and Paul R. C. Kent^{†,⊥}

[†]Center for Nanophase Materials Sciences, Oak Ridge National Laboratory, Oak Ridge, Tennessee 37831, United States, [‡]Université Paul Sabatier, CIRIMAT UMR CNRS 5085, 118 route de Narbonne, 31062 Toulouse, France, [§]Department of Materials Science and Engineering and A. J. Drexel Nanomaterials Institute, Drexel University, Philadelphia, Pennsylvania 19104, United States, and [⊥]Computer Science and Mathematics Division, Oak Ridge National Laboratory, Oak Ridge, Tennessee 37831, United States. ^{||}Present address: Materials Science and Technology Division, Oak Ridge National Laboratory, Oak Ridge, TN 37381, USA

ABSTRACT Rechargeable non-lithium-ion (Na^+ , K^+ , Mg^{2+} , Ca^{2+} , and Al^{3+}) batteries have attracted great attention as emerging low-cost and high energy-density technologies for large-scale renewable energy storage applications. However, the development of these batteries is hindered by the limited choice of high-performance electrode materials. In this work, MXene nanosheets, a class of two-dimensional transition-metal carbides, are predicted to serve as high-performing anodes for non-lithium-ion batteries by combined first-



principles simulations and experimental measurements. Both O-terminated and bare MXenes are shown to be promising anode materials with high capacities and good rate capabilities, while bare MXenes show better performance. Our experiments clearly demonstrate the feasibility of Na- and K-ion intercalation into terminated MXenes. Moreover, stable multilayer adsorption is predicted for Mg and Al, which significantly increases their theoretical capacities. We also show that O-terminated MXenes can decompose into bare MXenes and metal oxides when in contact with Mg, Ca, or Al. Our results provide insight into metal ion storage mechanisms on two-dimensional materials and suggest a route to preparing bare MXene nanosheets.

KEYWORDS: MXenes · energy storage · metal ion batteries · multilayer adsorption · conversion reaction · two-dimensional

Rechargeable Li-ion batteries (LIBs), one of the most important energy storage systems, have been widely used in portable electronic devices and are expected to power electric vehicles.¹ However, the large-scale electrical energy storage application of LIBs is hampered by concerns of limited lithium natural deposits, high production cost, and safety issues.^{2,3} In this regard, the development of new battery systems is urgently needed for the next generation of renewable energy technologies. Currently, rechargeable Na-ion,^{4,5} K-ion,^{6,7} Mg-ion,^{8–11} Ca-ion,^{12,13} and Al-ion^{14,15} batteries are attracting much attention due to their use of abundant elements, high theoretical capacities, suitable negative redox potentials, operational safety, and environmentally benign nature.

Similar to LIBs, the electrochemical performance of non-lithium-ion batteries (NLIBs) is highly dependent on the properties of the

electrolyte and electrode materials. Most existing studies of NLIBs are focused on developing cathode materials. A number of materials with large interstitial spaces, including layered transition-metal oxides,¹² olivine,¹⁶ and open framework materials,¹⁷ have been reported to show high capacities and good cyclabilities as cathodes. Compared with the fast improvement in cathode materials, the development of anode materials is much slower and limited to carbon-related materials and group IVA and VA element-based metal alloys that are promising anode materials for LIBs.^{18–25} Unfortunately, most of these materials do not work for NLIBs. For instance, graphite, the most commonly used anode material in LIBs, shows little or no electroactivity for NLIBs.²⁶ Other carbon materials^{18–20} show good cyclabilities at low rates with a capacity no higher than 300 mA h g⁻¹. On the other hand, metal alloys can deliver high capacities

* Address correspondence to yxe@ornl.gov; gogotsi@drexel.edu.

Received for review July 16, 2014 and accepted August 26, 2014.

Published online August 26, 2014 10.1021/nn503921j

© 2014 American Chemical Society

but at the cost of large volume expansion,^{21–25} which may eventually cause a failure of the electrode. Therefore, the development of high-performance anode materials with reversible and fast ion insertion/extraction and high capacities remains a major challenge for NLIBs.

Layered two-dimensional (2D) nanomaterials, such as graphene and the transition-metal dichalcogenides, are potential Li host materials with enhanced capacities and mobilities due to their unique open morphologies.^{27–33} The MoS₂/graphene composite paper has also been reported to be a promising anode material for Na-ion batteries.³⁴ Recently, a new class of 2D early-transition-metal carbides ($M_{n+1}C_n$), so-called MXenes, was discovered.^{35–37} The surfaces of MXene nanosheets are mainly covered by OH groups due to etching in acidic solutions. MXenes are good electrical conductors,^{35,36,38} may have high-capacity for hydrogen storage,³⁹ may be thermoelectric,⁴⁰ and show clear promise as energy storage^{41–46} materials. In particular, MXenes show high experimentally measured Li capacity (up to 410 mA h g⁻¹) and good rate capabilities.⁴¹ The X-ray adsorption spectra and theoretical simulations suggest that the surface structure of MXene nanosheets is the key enabler for Li storage, where OH groups are converted into O termination by high temperature annealing⁴⁴ and/or by metal adsorption^{44,47} for improved Li-ion storage. The high measured Li capacity may also be due to an unconventional Li multilayer adsorption.⁴⁴ More intriguingly, when MXenes are used as electrodes for electrochemical capacitors, unlike graphite, other metal ions, including Na⁺, K⁺, Mg²⁺, and Al³⁺, can be intercalated into MXenes.⁴² Hence, this opens the possibility to use MXenes as anode materials for NLIBs. Additionally, although the nonterminated (bare) MXenes are predicted to have attractive physical properties,^{39,43,46} there is no experimental or theoretical study on how to generate bare MXenes from terminated MXenes. There is also a need to explore possible methods for synthesizing bare MXenes. The aim of this study is to understand metal ion (Na⁺, K⁺, Mg²⁺, Ca²⁺, and Al³⁺) storage mechanisms on MXene nanosheets by combining first-principles simulations with select experimental measurements. We predict both O-terminated and bare MXenes are promising electrode materials for NLIBs. In particular, bare MXenes exhibit higher capacities and better rate capabilities than O-terminated ones. The experiments show that Na⁺ and K⁺ are cycleable with a terminated Ti₃C₂ nanosheet, which is consistent with theoretical calculations. Moreover, Mg and Al show exceptionally high theoretical capacities due to a storage mechanism of *stable* multilayer adsorption. We also propose a possible route to synthesize bare MXenes. Our findings are encouraging for further experimental and theoretical research.

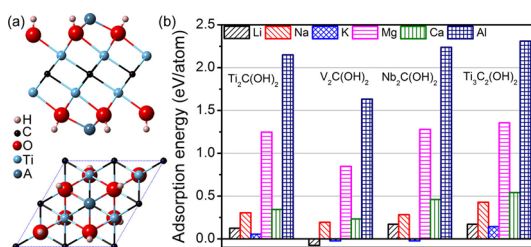


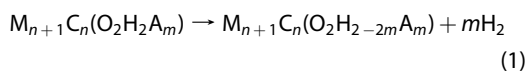
Figure 1. (a) Side and top views of ion adsorption on Ti₂C(OH)₂ nanosheet and (b) ion adsorption energies for OH-terminated MXene nanosheets.

RESULTS AND DISCUSSION

Metal Ion Storage on OH-Terminated MXene Nanosheets.

We start by considering metal ion adsorption on MXene nanosheets with OH termination. Not surprisingly, these metal ions have similar adsorption sites as Li (Figure 1a).⁴⁴ For a 2 × 2 MXene nanosheet, only two metal atoms can be adsorbed, showing $M_{n+1}C_n(OH)_2A_{0.5}$ (A is the adsorbed metal atom) stoichiometry. The distances between metal atoms and the nearest O atoms are 2.391, 3.094, 2.107, 2.308, and 1.989 Å for Na, K, Mg, Ca, and Al on Ti₂C(OH)₂ surfaces, respectively. Together with 1.941 Å for Li, the distances show a good correspondence to the ionic radii of the adsorbed atoms. The calculated adsorption energies are summarized in Figure 1b. Most of the adsorption energies are positive, suggesting these ions are not well adsorbed by OH-terminated MXenes. In particular, Mg and Al have much higher adsorption energies than other ions. This may relate to the strong Coulomb repulsion between them and the MXene Ti atoms. Ca should also show similar behavior, but the larger distance between Ca and Ti atoms reduces the Coulomb interaction, also reducing the adsorption energy. Nonetheless, the Mg and Al adsorption energies are lower than their calculated cohesive energies (1.519 eV/atom for Mg, 3.452 eV/atom for Al). They may still be physisorbed by OH-terminated MXenes.

Recent studies have shown that the surface H atoms can be removed by Li or Pb adsorption.^{44,47} We then check the stability of H atoms after metal ion adsorption following the proposed reaction:



The calculated reaction energy pathways on Ti₂C(OH)₂ are shown in Figure S1 (Supporting Information). Clearly, the final states have lower energies than the initial states, implying the reaction is exothermic and thermodynamically favorable. The calculated reaction barriers are 0.428, 0.382, 0.425, 0.239, and 0.385 eV for Na, K, Mg, Ca, and Al, respectively, which are close to the 0.503 eV for Li.⁴⁴ Therefore, H removal can also be expected with adsorption of these metal ions. It follows that OH-terminated MXene nanosheets are not desired for metal ion storage, just like Li.

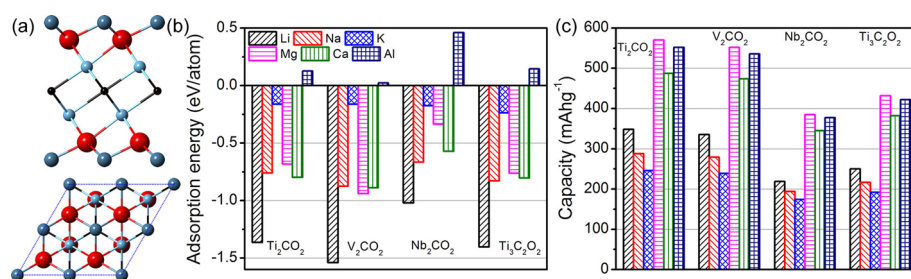


Figure 2. (a) Side and top views of ion adsorption on Ti_2CO_2 nanosheet, (b) ion adsorption energies, and (c) theoretical capacities on O-terminated MXene nanosheets. For the Al capacity on Nb_2CO_2 , we use the same coverage as other MXenes.

Metal Ion Storage on O-Terminated MXene Nanosheets.

Figure 2b shows the ion adsorption energies that are calculated assuming $\text{M}_{n+1}\text{C}_n\text{O}_2\text{A}_2$ stoichiometry with a full adsorption layer (Figure 2a). All the adatoms, except for Al, have negative adsorption energies, indicating they can form a full adsorption layer on O-terminated MXenes. The positive adsorption energy of Al suggests that it is either physisorbed or partially chemisorbed. We then examine how the adsorption energy varies with increasing Al concentration. We find that, up to 2/3 Al coverage, Ti_2CO_2 , V_2CO_2 , and $\text{Ti}_3\text{C}_2\text{O}_2$ nanosheets have a negative adsorption energy of -0.202 , -0.681 , and -0.266 eV/atom, respectively, which corresponds to a stoichiometry of $\text{M}_{n+1}\text{C}_n\text{O}_2\text{A}_{4/3}$. For Nb_2CO_2 nanosheet, Al always has a positive adsorption energy. This may be induced by the strong interaction between metal adatom and Nb atoms—the metal ion adsorption energies on Nb_2CO_2 nanosheet are higher than for other MXenes. Therefore, Al should be physisorbed on Nb_2CO_2 . We explain this difference as follows: These adatoms act as n-type dopants on O-terminated MXene nanosheets. From Bader charge analysis, we find that Na, K, Mg, Ca, and Al transfer 0.45, 0.48, 0.76, 0.79, and 1.09 e /atom, respectively, to O atoms on Ti_2CO_2 surfaces (Figure S2, Supporting Information). Since each Al atom can donate more electrons than other adatoms, fewer Al adatoms are required to fulfill the O bands. The increased repulsion on adding further Al atoms thus causes the instability for a full Al adsorption layer.

In Figure 2c, we show the capacities of MXene nanosheets corresponding to their coverage. The theoretical capacities of multivalent metal ions are obviously higher than the monovalent ions, simply because they are carrying additional charges. Ti_2CO_2 shows the highest capacity at 288, 264, 570, 487, and 552 mAhg^{-1} for Na, K, Mg, Ca, and Al, respectively (the gravimetric capacity includes the weight of the adsorbed metal ions as shown in Methods). The difference between metal ions with the same valence state is in part due to their different atomic weights. The heavier ions will have lower gravimetric capacity. Although the calculated capacities of monovalent ions are close to those of carbon related materials,^{18,19,48} the capacities of multivalent atoms stand out. For instance, the calculated Mg

capacities are close to the theoretical capacities of its alloy anodes (Table S11, Supporting Information).^{24,25} The capacity of Ca is even comparable with the predicted high capacity of defective graphene (Table S11, Supporting Information).⁴⁹ We have to mention that a proper electrolyte is essential to obtain optimal performance for these metal ion batteries, especially for the multivalent ions.⁵⁰

Previous work has shown that Li may form more than one layer on $\text{Ti}_3\text{C}_2\text{O}_2$ surfaces to enhance the Li capacity.⁴⁴ To check this possibility of metal multilayer adsorption on O-terminated MXene nanosheets, we calculate the second layer ($\text{M}_{n+1}\text{C}_n\text{O}_2\text{A}_2\text{A}_2$, Figure 3a) adsorption energies for the various adatoms (Figure 3b). Al is not included since it cannot even form a full first layer. Interestingly, these metal ions behave quite differently. We divide them into three groups: (1) K with the most positive adsorption energy (>0.6 eV/atom); (2) Li, Na, and Ca with moderate positive adsorption energies (0–0.4 eV/atom); and (3) Mg with a negative adsorption energy. It is very unlikely that K can be adsorbed on already potasiated MXenes. Similar to Li, Na and Ca may form partial layers. Surprisingly, the second Mg layer is *thermodynamically stable* on top of magnesiated MXenes. Further investigation shows another Mg layer can be added before the adsorbed Mg shows bulk behavior (Figure S3, Supporting Information). Not surprisingly, the Mg capacity increases with the number of adsorbed Mg layers (Figure 3c). However, the increase becomes smaller with each additional layer because of the increased weight. Compared with other metal ions, Mg has a more complicated storage mechanism on O-terminated MXenes due to the presence of the stable extra Mg adsorption layers. Besides the normal insertion/extraction of the first Mg layer, other layers have the plating/stripping mechanism similar to Mg metal anodes.^{8,9} It is well-known that a nonconductive layer will form on the Mg metal surface in conventional nonaqueous electrolytes, which are widely used in LIBs.^{51,52} However, this may be avoided by plating Mg on MXene surfaces, since the latter has shown good electrical conductivity with nonaqueous electrolytes for LIBs.⁴¹ Moreover, distinct from Li, Mg will not form dendrites that can result in cell damage.⁹ Thus, the unique stable multilayer adsorption ensures the high

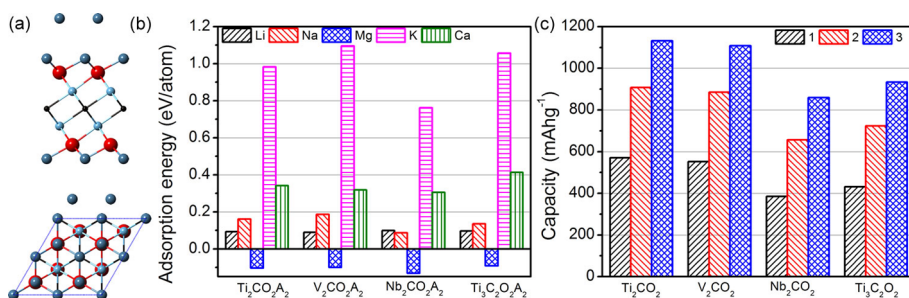


Figure 3. (a) Side and top views of ion adsorption on a metalated Ti_2CO_2 nanosheet; (b) second metal layer adsorption energies for $M_{n+1}C_nO_2A_2$; (c) Mg capacity variation as a function of adsorbed number of Mg layers.

Mg capacity on O-terminated MXene nanosheets if the overall kinetics allow and a stable electrolyte is utilized.

Electrochemical measurements are performed to test the feasibility of using MXene nanosheets as anodes for NLIBs. Figure 4 shows cyclic voltammeteries (CVs) and the change of the capacities vs cycle number calculated from galvanostatic charge–discharge experiments, for multilayer $Ti_3C_2T_x$ ($T = O, F,$ and/or OH) anodes in Na-ion- and K-ion-containing electrolytes. The capacity–voltage curves (Figure 4a,c) show irreversible peaks below 1.2 V vs Na^+/Na and below 1.5 V vs K^+/K during charging in both electrolytes, originating from the formation of a solid electrolyte interphase (SEI).⁴⁵ Na-ion intercalation (Figure 4b) shows a first cycle discharge capacity at 370 mA h g^{-1} , which is significantly higher than the predicted Na capacity with one Na adsorption layer (217 or 268 mA h g^{-1} , including or excluding the weight of adsorbed metal ions). This is most likely due to the formation of SEI layer and the adsorption of extra Na ions as similarly observed for Li-ion intercalation.⁴⁴ On the other hand, the initial discharge capacity of K-ion intercalation is 260 mA h g^{-1} (Figure 4d) that is close to the predicted one (192 or 268 mA h g^{-1} , including or excluding the weight of adsorbed metal ions). Noteworthy, the initial charge capacities of Na- and K-ion intercalation are 164 and 146 mA h g^{-1} , respectively. The large irreversible capacity loss (56% for Na^+ and 43% for K^+) in the first cycle can be mainly attributed to irreversible processes, such as reactions between Na^+ or K^+ with water or unwashed etching products from the synthesis and the formation of SEI. The reversible Na and K capacities decrease to 80 and 45 mA h g^{-1} , respectively, after 120 cycles. We have to mention that the experimentally measured initial discharge capacities of Li-, Na- and K-ion batteries are 430 ,⁴¹ 370 , and 260 mA h g^{-1} , respectively, corresponding to 3.25 Li, 2.79 Na, 1.96 K per $Ti_3C_2T_x$. This follows the order of the ionic radii ($0.76, 1.06,$ and 1.38 \AA for $Li^+, Na^+,$ and K^+ , respectively). Surprisingly, regardless of the size of the ions, Li-, Na-, and K-ion batteries have similar capacities for the next cycles up to 10 cycles around 100 mA h g^{-1} , approximately 0.75 ion hosted reversibly per $Ti_3C_2T_x$. The Li and Na capacities remain similar up to 120 cycles, while the K

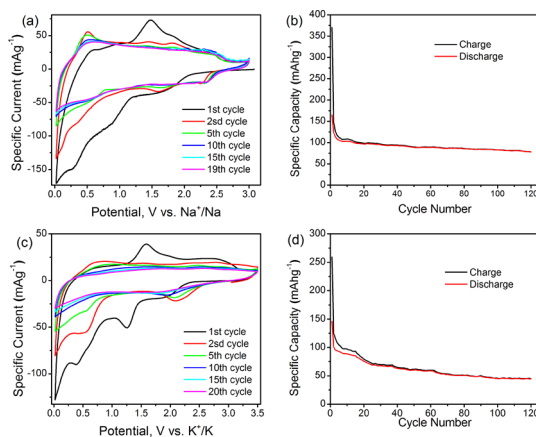


Figure 4. Electrochemical testing of terminated Ti_3C_2 : cyclic voltammetry at 0.2 mV s^{-1} and specific capacities vs cycle number at 0.1 Ag^{-1} in Na-ion battery (a, b) and K-ion battery (c, d) in 1 M NaClO_4 and 1 M KPF_6 electrolyte, respectively.

capacity is reduced. This is most likely because electrode deformation of electrode material increases and the kinetics decrease as the ion size increases, as observed in other electrode materials studied for Li-, Na-, and K-ion batteries.^{53,54} The current experiments clearly show the feasibility of large ion storage in MXene nanosheets, which is consistent with theoretical predictions. Moreover, these experiments are performed with unoptimized materials. Further experimental efforts are expected to improve the performance of MXene in NLIBs by using delaminated MXenes as anodes and by selecting or developing better electrolytes, especially for multivalent ions.

Mechanism of Multilayer Adsorption. To obtain insights on the physical origin of the predicted multilayer adsorption behavior, we analyze the electronic structures of Ti_2CO_2 with two metal layers. Figure 5 shows the electron localization functions (ELF) of (110) section and the projected density of states (PDOS). Apart from the adsorption energies, the electronic structures for adsorbed Li, Na, and Mg are quite similar. K and Ca also display similarity. For Li, Na, and Mg, the electrons are spread out in the metal layers forming a negative electron cloud⁵⁵ (NEC, Figure 5a–c), in other words, metallic bonds, similar to their bulk counterparts. NEC

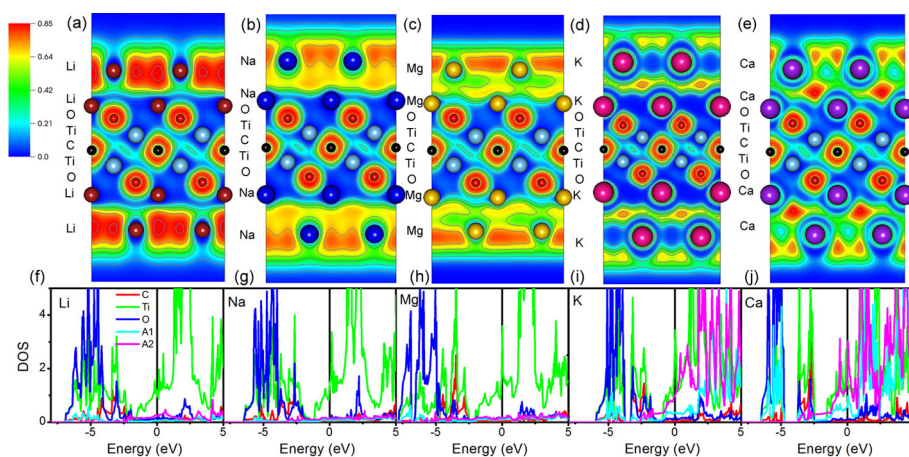


Figure 5. (a–e) Electron localization functions of (110) section for Li, Na, Mg, K, and Ca, respectively, and (f–j) corresponding projected density of states of Ti_2CO_2 with two metal layers adsorbed.

can screen the repulsion between the positive metal ions (adatom–adatom and Ti–adatom), therefore, to stabilize the second-layer adsorption. Moreover, hybridization between adatoms and Ti orbitals in the vicinity of the Fermi level is almost nonexistent (Figure 5f–h), indicating weak repulsive interactions between Ti and Li, Na, and Mg, which may further decrease the adsorption energy. Since Mg has two valence electrons compared with one for Li and Na, the screening effect of NEC may be stronger in Mg than in Li and Na. Thus, the second Mg layer has a negative adsorption energy compared with the positive adsorption energies of Li and Na (Figure 2b). In the case of K and Ca, the electrons are more localized (Figure 5d,e). This may be due to electron transfer from spherical *s* orbitals to more localized nonspherical *p* or *d* orbitals. Similarly, the screening effects of NEC in K should be weaker than that of Ca. From the PDOS (Figure 5i,j), we observe that even the first K and Ca layer has some contributions to the DOS near the Fermi level, indicating a repulsive interaction between them and Ti atoms. However, the K–O and Ca–O bonds help the adsorption of the first layer. Since Ca can transfer more charge to O than K, the Ca–O bond is stronger than the K–O bond. Thus, K has the highest adsorption energy among all the metal ions (except for Al) for the first layer (Figure 2b). Furthermore, both K and Ca show strong hybridization with Ti for the second layer. This remarkable repulsion largely increases the adsorption energy for the second K and Ca layer. Hence, even after the screening effect is considered, K has the most positive adsorption energy for the second layer, and Ca has an adsorption energy lower than K but higher than other alkali metals (Figure 3b).

To validate our effective screening arguments, we compare the vertical distances between two metal layers adsorbed on Ti_2CO_2 with the same distances in their bulk metals (Figure S4, Supporting Information). It is clear that Mg has the smallest difference at $\sim 5\%$,

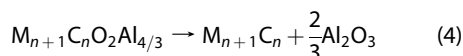
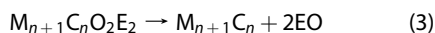
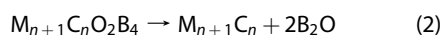
indicating a minimal repulsion between the positive ions due to the strong screening effect. Ca has a larger distance difference at 24%, followed by Li and Na around 55%. Although the NEC is more localized in Ca than Li and Na, it still can screen most of the repulsive interactions. K has the largest distance difference at 65% corresponding to the weak screening effect. Therefore, the distance differences match well with our proposed screening effect, which is critical for the multilayer adsorption.

From the above analysis, we have formulated some criteria for the formation of stable multilayer adsorption on MXene nanosheets: (i) low adsorption energy of the first layer (minimal repulsion between the MXene transition metal atoms and the adatoms); (ii) small contribution to the DOS near the Fermi level from the extra layers (to minimize the repulsion induced by the extra layers); (iii) strong screening effects from the NEC. Although Al may also show strong screening effects, it cannot form the first full layer. Thus, Mg might be the only light metal ion to show multilayer adsorption on O-terminated MXenes.

Ion Diffusion on O-Terminated MXenes. A high-performance anode material should not only have high capacity, but also have good rate capability. We then shift our attention to the motion of metal ions on O-terminated MXenes. For Mg, we only consider the first layer, which will govern performance. Diffusion on an already adsorbed first metal layer should be easier. Figure S5 (Supporting Information) shows the diffusion pathways and energies of single metal adatoms moving between two equivalent adsorption sites using the NEB method. The diffusion barriers of monovalent metal adatoms are distinguishable from multivalent metal adatoms. The former have a low energy barrier (<0.3 eV, comparable with Li); the latter have a high energy barrier (>0.5 eV) because of their stronger interaction with O atoms. The only exception is Al on Nb_2CO_2 , where it is physisorbed. Since the diffusion barrier may increase at high coverage, the mobilities of multivalent

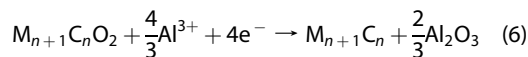
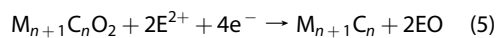
adatoms should further decrease. This suggests that, on O-terminated MXene nanosheets, Na and K should have moderate capacities with good rate capabilities as shown in the experiments. Mg, Ca, and Al may possess high capacities, but their rate performances will not be as good as the monovalent metal ions.

Decomposition of O-Terminated MXenes. Studies have shown that some transition-metal oxides (TMO), such as FeO, NiO, and CoO,⁵⁶ and dichalcogenides (TMDC), such as MoS₂ and WS₂,²⁹ can deliver high Li capacities for LIBs by conversion reactions forming Li₂O or Li₂S and transition metals. The conversion reaction can transfer more electrons than the conventional intercalation reaction to enhance the Li storage. Although this Li-ion involved conversion reaction has not been observed in MXene-based LIBs,⁴⁴ we cannot rule out the possibility for other metal ions, especially for multivalent ones, where the propensity to form metal oxides was delineated. To investigate the potential conversion reactions, we propose the following decomposition reactions



where B represents alkali metals and E stands for alkali-earth metals. The calculated energy differences between right and left side of the equations are shown in Figure 6a.

Clearly, reactions 3 and 4 are thermodynamically favorable. The O-terminated MXenes are more like to decompose into bare MXenes and metal oxides in the presence of Mg, Ca, or Al, as illustrated in Figure S6 (Supporting Information). Then reactions 3 and 4 can be rewritten as



The reason why only multivalent metals can strip O atoms away is straightforward. When metal adatoms donate charges to O atoms, in order to keep electro-neutrality, fewer electrons are transferred from transition metals to the O atoms in MXenes. As mentioned above, multivalent metal adatoms can transfer more charge to O atoms than monovalent metal adatoms (Figure S2, Supporting Information); thus, the TM–O bonds with Mg, Ca, and Al adsorption should be weaker than with Li, Na, and K adsorption. Hence, the TM–O bonds are easier to break with multivalent adatoms.

Since our simulations are performed at 0 K, it is necessary to check the viability of these reactions at

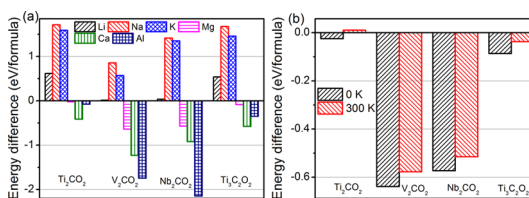


Figure 6. Energy differences of (a) reactions 2–4 and (b) reaction 3 at 0 and 300 K for Mg.

300 K. We calculate the Gibbs free energy differences for reaction 3 as an example (Figure 6b). The energy differences only increase by 0.05 eV/formula at 300 K, suggesting temperature has a minor effect. Thus, the MXene reduction is still thermodynamically favorable at ambient conditions. Another important factor is the kinetics. Unfortunately, we are unable to estimate the energy barriers for these reactions because we have insufficient knowledge of the initial and final states. Whether these reactions are reversible is also unclear, although MgO (10.603 eV/formula), CaO (11.618 eV/formula), and Al₂O₃ (32.079 eV/formula) have similar cohesive energies per electron as Li₂O (12.231 eV/formula). Nevertheless, we identify a possible route to synthesize bare MXenes even with the presence of metal oxides.

Metal Ion Storage on Bare MXene Nanosheets. Unlike the transition metals, bare MXene nanosheets are capable of storing Li ions.^{43,46} We then move to investigate the metal ion storage on bare MXenes. Figure 7b shows the adsorption energies of metal adatoms forming a full layer on M_{n+1}C_n (Figure 7a). We immediately observe the different adsorption behavior between bare and O-terminated MXenes. K cannot form a full layer on any of the bare MXenes; the maximal stable coverage is only 2/3. Meanwhile, Ca can only form a full layer on Nb₂C. For other MXenes, the coverage is 1/2. In contrast, Al, which cannot form a stable full layer on O-terminated MXenes, is able to form a full layer on bare MXenes. This difference should originate from the different electronic properties. In Figure S7 (Supporting Information) we show the ELF_s and PDOS of Ti₂CA₂. The ELF_s are very much like the ELF_s of multimetal layers adsorbed on O-terminated MXenes. However, without surface O atoms, the metal adatoms are no longer electron donors. The adsorbed metal layer is stabilized by the screening effect of NEC rather than A–O bonds. K and Ca adatoms still strongly hybridize with Ti (Figure S7c,e, Supporting Information), and there are no more O atoms to help them be adsorbed. Therefore, they have higher adsorption energies than those on O-terminated MXenes. An interesting feature of Ca is the stable adsorption layer on Nb₂C. The PDOS shows that the magnitude of hybridization between Nb and Ca, especially at the Fermi level, is smaller than other transition metals (Figure S8, Supporting Information). Hence, the repulsion between Nb and Ca is weaker and may be screened by NEC. Al, on the other hand,

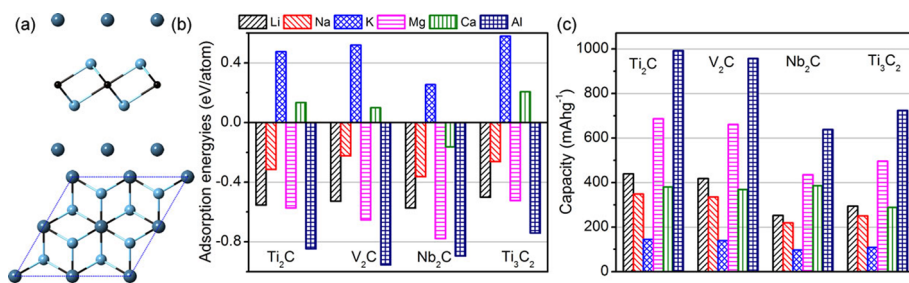


Figure 7. (a) Side and top views of ion adsorption on Ti_2C nanosheets. (b) Ion adsorption energies and (c) theoretical capacities on M_{n+1}C_n . For the K and Ca capacities, we use their actual coverage for each MXene.

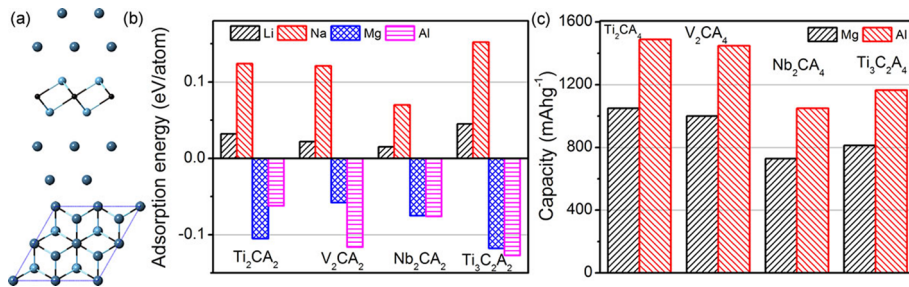


Figure 8. (a) Side and top views of ion adsorption on Ti_2CA_2 nanosheet. (b) Ion adsorption energies on $\text{M}_{n+1}\text{C}_n\text{A}_2$. (c) Theoretical Mg and Al capacities with two metal layers.

shows small repulsion with Ti (Figure S71, Supporting Information) and a well-distributed NEC (Figure S7f, Supporting Information). Therefore, it can easily be adsorbed. The corresponding metal capacities are shown in Figure 7c. Because of their reduced weight, the capacities are higher than O-terminated MXenes. For Al, it reaches as high as 992 mA h g^{-1} on Ti_2C , which is one of the highest capacities predicted for the Al-ion battery. Mg also shows a high capacity of 687 mA h g^{-1} on Ti_2C , which is higher than the theoretical capacity of Sn (Table S11, Supporting Information).

With one metal layer, bare MXenes already show promise as high-capacity anode materials for NLIBs, especially for Mg- and Al-ion batteries. It is worth noting that, using our proposed criteria, Mg and Al may form stable multilayers on bare MXenes. We then examine this possibility together with Li and Na. Figure 8b summarizes the second metal layer adsorption energies on $\text{M}_{n+1}\text{C}_n\text{A}_2$. As expected, Mg and Al can form stable second adsorption layer on all bare MXenes, while Li and Na cannot. From the electronic structures (Figure S9, Supporting Information), we find that Li and Na are quite similar to Mg and Al. One possible explanation for the different behavior is the strength of the screening effect induced by NEC. Similar to O-terminated MXenes, Li and Na have weaker screening effect than Mg and Al, and are more likely to form a partial layer on top of the first adsorption layer instead of a stable full layer. Again, Mg and Al can form up to three metal layers on bare MXene nanosheets. The Mg and Al capacities with two metal layers are shown in Figure 8c. Both of them exhibit high

theoretical capacities (1488 and 1050 mA h g^{-1} for Al and Mg, respectively). Moreover, Al, like Mg, should not form dendrites with plating.⁵⁷ The multilayer adsorption can greatly increase capacity with a smaller safety concern than for alkali metals.

Since most of the interactions between metal adatoms and surface transition metal atoms are screened by NEC, the diffusion of metal atoms on bare MXenes is expected to be faster than on O-terminated MXenes.^{43,44} Figure S10 (Supporting Information) shows diffusion energy pathways of single metal adatoms on bare MXenes. It also has a similar diffusion pathway as O-terminated MXenes. As we predicted, the diffusion energy barriers are much lower than the O-terminated MXenes. Most of the metal adatoms have an energy barrier lower than 0.1 eV . Al has a slightly higher energy barrier, but not larger than 0.15 eV . Such low diffusion barrier should result in excellent high rate performance of bare MXenes.

Our simulations suggest MXenes have a more complicated metal ion storage mechanism than other anode materials, especially for multivalent ions. Starting with the OH-terminated MXenes, we will first obtain the O termination. Then the O-terminated MXenes may react to form bare MXenes and metal oxides upon metalization through the proposed conversion reactions. If these reactions are reversible, the metal ions will be stored in the form of metal oxides first. Next, metal ions could intercalate into bare MXenes to form the first metal layer (for most of the metal ions this will be the only adsorption layer). Finally, for Mg and Al, they can store more ions by forming multimetal layers to further increase the capacity. Therefore, all the known

storage mechanisms, including reversible conversion reactions, insertion/extraction, and plating/stripping, may be found in MXenes. The high capacities and low diffusion barriers make MXene nanosheets unique materials for metal ion storage, particularly, for Mg and Al. Our identification of possible electrode materials highlights the urgent need to discover suitable electrolytes. The latter now appears to be the key missing component to enable NLIBs application of MXenes. More efforts are needed to design appropriate electrolytes. For bare MXenes, this is even more critical since bare MXenes have greater reactivity than terminated MXenes due to their surface dangling bonds.

CONCLUSIONS

We have systematically investigated the Na, K, Mg, Ca, and Al storage on MXene nanosheets using first-principles simulations. Our results show that both O-terminated and bare MXene nanosheets are promising electrode materials for NLIBs. Bare MXenes have

higher capacities and greater ion mobilities than the O-terminated MXenes. The theoretical predictions are supported by experimental results for Na- and K-ion intercalation of terminated MXenes. Moreover, O-terminated MXenes are expected to decompose into bare MXenes and metal oxides in contact with multivalent metals. We also find that MXene nanosheets can store Mg and Al multilayer showing a combined conversion reaction, insertion/extraction, and plating/stripping metal ion storage mechanism, if the kinetics allow. Several rules have been summarized for the formation of stable multilayer. This study also provides the first theoretical pathway to bare MXenes from O terminated ones and sheds light on the counterintuitive metal ion storage mechanism on MXenes. It is important to note that a proper electrolyte is crucial for enabling the application of MXene nanosheets as anodes for multivalent ion batteries. Future experiments are desired to test MXenes as anode materials for rechargeable multivalent-ion batteries and to validate our predictions.

METHODS

Density Functional Theory Simulation. First-principles calculations are carried out using density functional theory (DFT)⁵⁸ and the all-electron projected augmented wave (PAW) method⁵⁹ as implemented in the Vienna *ab initio* simulation package (VASP).⁶⁰ For the exchange-correlation energy, we use the Perdue–Burke–Ernzerhof (PBE) version of the generalized gradient approximation (GGA).⁶¹ The van der Waals (vdW) density functional (vdW-DF) of optB86b are considered for all simulations.⁶² A plane-wave cutoff energy of 580 eV is sufficient to ensure convergence of the total energies to 1 meV per primitive cell. The underlying structural optimizations are performed using the conjugate gradient method, and the convergence criterion was set to 10^{-5} eV/cell in energy and 0.005 eV/in force. The Brillouin zone (BZ) was integrated using a $12 \times 12 \times 1$ Monkhorst–Pack⁶³ (MP) *k*-point grid during the relaxation and a denser $24 \times 24 \times 2$ MP mesh for the density of states (DOS) calculations. The vacuum separation between two nanosheets was set to 15 Å to avoid any interaction due to the use of periodic boundary conditions. Metal adsorptions are studied on a $2 \times 2 \times 1$ and/or $3 \times 3 \times 1$ MXene nanosheet with a BZ sampling of $8 \times 8 \times 1$ and/or $6 \times 6 \times 1$ *k*-mesh, respectively. The adsorption energies of the first layer is calculated with

$$E_{\text{ad}} = (E_{\text{MXene}+A_n} - E_{\text{MXene}} - nE_A)/n$$

where $E_{\text{MXene}+A_n}$ is the total energy of a metalated nanosheet, E_{MXene} denotes the total energy of pristine MXene nanosheet, E_A is the total energy of bulk metal, and n presents the number of adsorbed metal adatoms. For additional layers, the adsorption energies are calculated using the expression

$$E_{\text{ad}} = (E_{\text{MXene}+A_n+A_m} - E_{\text{MXene}+A_n} - mE_A)/m$$

where the total energy of metalated nanosheet is used as energy reference instead of pristine nanosheet. In this scheme, the lower the adsorption energy, the stronger the binding between adsorbent and adsorber. The metal capacities are estimated from

$$C_A = \frac{n_A Z_A F}{M_{\text{MXene}} + nM_A}$$

where n_A is the number of adsorbed metal adatoms, Z_A is the valence state of metal adatoms, F is the Faraday constant (26801 mAh/mol), M_{MXene} is the mole weight of MXene

nanosheet, and M_A is the mole weight of metal adatoms. Note, the weight of the adsorbed metal adatom is not considered for most of the calculated capacities presented in literatures. The cohesive energies are calculated by

$$E_{\text{coh}} = E_{A_n B_m} - nE_A - mE_B$$

where $E_{A_n B_m}$ is the total energy of the compound and E_A and E_B are the energies of isolated atoms.

Transition-State Searching. To determine the energy barriers and minimum energy paths of surface reactions and metal diffusion, we use the climbing image nudged elastic band method (CI-NEB)⁶⁴ implemented in VASP. A $2 \times 2 \times 1$ MXene nanosheet with a BZ sampling of $8 \times 8 \times 1$ is used for the transition state searching. The NEB path is first constructed by linear interpolation of the atomic coordinates and then relaxed until the forces on all atoms were <0.05 eV/Å. Six to eight images are simulated between initial and final states.

Gibbs Free Energy Calculation. We have employed the so-called quasi-harmonic approximation to calculate the thermal properties at constant pressure. Gibbs free energies at finite temperatures are obtained as the minimum values of the thermodynamic functions from the Vinet equation of state.⁶⁵ Phonon calculations were performed by the supercell approach. Real-space force constants of supercells were calculated in the density-functional perturbation theory⁶⁶ (DFPT) implemented in the VASP code, and phonon frequencies were calculated from the force constants using the PHONOPY⁶⁷ code. A $3 \times 3 \times 1$ supercell and $6 \times 6 \times 1$ MP *k*-grid is used to generate the force constants.

Electrochemical Characterization. Electrochemical measurements were done in a two-electrode Swagelok cells by cyclic voltammetry at 0.2 mV s^{-1} and galvanostatic charge–discharge cycling at 0.1 Ag^{1-} using a VMP3 potentiostat (Biologic, S.A.). The working electrodes were a mixture of 80 wt % of Ti_3C_2 and 20 wt % carbon black. The cells were assembled in an argon-filled glovebox using Na or K metals as counter electrode and separated by a glass fiber separator (Whatman GF/A) saturated with either 1 M NaClO_4 or 1 M KPF_6 solutions in EC:PC (1:1 in weight).

Conflict of Interest: The authors declare no competing financial interest.

Acknowledgment. We thank P.-L. Taberna and P. Simon for useful discussions. This work was supported as part of the Fluid Interface Reactions, Structures and Transport (FIRST) Center, an Energy Frontier Research Center funded by the US Department

of Energy, Office of Science, Office of Basic Energy Sciences. This research used resources of the National Energy Research Scientific Computing Center, which is supported by the Office of Science of the US Department of Energy under Contract No. DE-AC02-05CH11231.

Supporting Information Available: The number of adsorption energies and capacities, the charges of metal adatoms on O terminated MXenes, the distances between metal layers, the diffusion pathways, the decomposition scheme of O terminated MXenes, and the calculated ELFs and PDOS of metal adsorption on bare MXenes. This material is available free of charge via the Internet at <http://pubs.acs.org/>.

REFERENCES AND NOTES

- Armand, M.; Tarascon, J.-M. Building Better Batteries. *Nature* **2008**, *451*, 652–657.
- Goodenough, J. B.; Park, K.-S. The Li-Ion Rechargeable Battery: a Perspective. *J. Am. Chem. Soc.* **2013**, *135*, 1167–1176.
- Tarascon, J.-M. Is Lithium the New Gold? *Nat. Chem.* **2010**, *2*, 510–510.
- Palomares, V.; Serras, P.; Villaluenga, I.; Hueso, K. B.; Carretero-González, J.; Rojo, T. Na-Ion Batteries, Recent Advances and Present Challenges to Become Low Cost Energy Storage Systems. *Energy Environ. Sci.* **2012**, *5*, 5884–5901.
- Slater, M. D.; Kim, D.; Lee, E.; Johnson, C. S. Sodium-Ion Batteries. *Adv. Funct. Mater.* **2013**, *23*, 947–958.
- Eftekhari, A. Potassium Secondary Cell Based on Prussian Blue Cathode. *J. Power Sources* **2004**, *126*, 221–228.
- Wessells, C. D.; Huggins, R. A.; Cui, Y. Copper Hexacyanoferrate Battery Electrodes With Long Cycle Life and High Power. *Nat. Commun.* **2011**, *2*, 550.
- Yoo, H. D.; Shterenberg, I.; Gofer, Y.; Gershinsky, G.; Pour, N.; Aurbach, D. Mg Rechargeable Batteries: an On-Going Challenge. *Energy Environ. Sci.* **2013**, *6*, 2265–2279.
- Aurbach, D.; Lu, Z.; Schechter, A.; Gofer, Y.; Gizbar, H.; Turgeman, R.; Cohen, Y.; Moshkovich, M.; Levi, E. Prototype Systems for Rechargeable Magnesium Batteries. *Nature* **2000**, *407*, 724–727.
- Amir, N.; Vestfrid, Y.; Chusid, O.; Gofer, Y.; Aurbach, D. Progress in Nonaqueous Magnesium Electrochemistry. *J. Power Sources* **2007**, *174*, 1234–1240.
- Doe, R. E.; Han, R.; Hwang, J.; Gmitter, A. J.; Shterenberg, I.; Yoo, H. D.; Pour, N.; Aurbach, D. Novel Electrolyte Solutions Comprising Fully Inorganic Salts with High Anodic Stability for Rechargeable Magnesium Batteries. *Chem. Commun.* **2014**, *50*, 243–245.
- Amatucci, G.; Badway, F.; Singhal, A.; Beaudoin, B.; Skandan, G.; Bowmer, T.; Piltz, I.; Pereira, N.; Chapman, T.; Jaworski, R. Investigation of Yttrium and Polyvalent Ion Intercalation into Nanocrystalline Vanadium Oxide. *J. Electrochem. Soc.* **2001**, *148*, A940–A950.
- Wang, R. Y.; Wessells, C. D.; Huggins, R. A.; Cui, Y. Highly Reversible Open Framework Nanoscale Electrodes for Divalent Ion Batteries. *Nano Lett.* **2013**, *13*, 5748–5752.
- Jayaprakash, N.; Das, S.; Archer, L. The Rechargeable Aluminum-Ion Battery. *Chem. Commun.* **2011**, *47*, 12610–12612.
- Li, Q.; Bjerrum, N. J. Aluminum as Anode for Energy Storage and Conversion: A Review. *J. Power Sources* **2002**, *110*, 1–10.
- Moreau, P.; Guyomard, D.; Gaubicher, J.; Boucher, F. Structure and Stability of Sodium Intercalated Phases in Olivine FePO₄. *Chem. Mater.* **2010**, *22*, 4126–4128.
- Lu, Y.; Wang, L.; Cheng, J.; Goodenough, J. B. Prussian Blue: a New Framework of Electrode Materials for Sodium Batteries. *Chem. Commun.* **2012**, *48*, 6544–6546.
- Cao, Y.; Xiao, L.; Sushko, M. L.; Wang, W.; Schwenzler, B.; Xiao, J.; Nie, Z.; Saraf, L. V.; Yang, Z.; Liu, J. Sodium Ion Insertion in Hollow Carbon Nanowires for Battery Applications. *Nano Lett.* **2012**, *12*, 3783–3787.
- Alcántara, R.; Jiménez-Mateos, J. M.; Lavela, P.; Tirado, J. L. Carbon Black: a Promising Electrode Material for Sodium-Ion Batteries. *Electrochem. Commun.* **2001**, *3*, 639–642.
- Tang, K.; Fu, L.; White, R. J.; Yu, L.; Titirici, M.-M.; Antonietti, M.; Maier, J. Hollow Carbon Nanospheres with Superior Rate Capability for Sodium-Based Batteries. *Adv. Energy Mater.* **2012**, *2*, 873–877.
- Darwiche, A.; Marino, C.; Sougrati, M. T.; Fraisse, B.; Stievano, L.; Monconduit, L. Better Cycling Performances of Bulk Sb in Na-Ion Batteries Compared to Li-Ion Systems: an Unexpected Electrochemical Mechanism. *J. Am. Chem. Soc.* **2012**, *134*, 20805–20811.
- Zhu, Y.; Han, X.; Xu, Y.; Liu, Y.; Zheng, S.; Xu, K.; Hu, L.; Wang, C. Electrospun Sb/C Fibers for a Stable and Fast Sodium-Ion Battery Anode. *ACS Nano* **2013**, *7*, 6378–6386.
- Qian, J.; Xiong, Y.; Cao, Y.; Ai, X.; Yang, H. Synergistic Na-Storage Reactions in Sn₄P₃ as a High-Capacity, Cycle-stable Anode of Na-Ion Batteries. *Nano Lett.* **2014**, *14*, 1865–1869.
- Shao, Y.; Gu, M.; Li, X.; Nie, Z.; Zuo, P.; Li, G.; Liu, T.; Xiao, J.; Cheng, Y.; Wang, C.; et al. Highly Reversible Mg Insertion in Nanostructured Bi for Mg Ion Batteries. *Nano Lett.* **2013**, *14*, 255–260.
- Singh, N.; Arthur, T. S.; Ling, C.; Matsui, M.; Mizuno, F. A High Energy-Density Tin Anode for Rechargeable Magnesium-Ion Batteries. *Chem. Commun.* **2012**, *49*, 149–151.
- Ge, P.; Fouletier, M. Electrochemical Intercalation of Sodium in Graphite. *Solid State Ionics* **1988**, *28*, 1172–1175.
- Chhowalla, M.; Shin, H. S.; Eda, G.; Li, L.-J.; Loh, K. P.; Zhang, H. The Chemistry of Two-Dimensional Layered Transition Metal Dichalcogenide Nanosheets. *Nat. Chem.* **2013**, *5*, 263–275.
- Zhao, X.; Hayner, C. M.; Kung, M. C.; Kung, H. H. Flexible Holey Graphene Paper Electrodes with Enhanced Rate Capability for Energy Storage Applications. *ACS Nano* **2011**, *5*, 8739–8749.
- Xiao, J.; Choi, D.; Cosimbescu, L.; Koech, P.; Liu, J.; Lemmon, J. P. Exfoliated MoS₂ Nanocomposite as an Anode Material for Lithium Ion Batteries. *Chem. Mater.* **2010**, *22*, 4522–4524.
- Jing, Y.; Zhou, Z.; Cabrera, C. R.; Chen, Z. Graphene, Inorganic Graphene Analogs and Their Composites for Lithium Ion Batteries. *J. Mater. Chem. A* **2014**, *2*, 12104–12122.
- Tang, Q.; Zhou, Z. Graphene-Analogous Low-Dimensional Materials. *Prog. Mater. Sci.* **2013**, *58*, 1244–1315.
- Li, Y.; Wu, D.; Zhou, Z.; Cabrera, C. R.; Chen, Z. Enhanced Li Adsorption and Diffusion on MoS₂ Zigzag Nanoribbons by Edge Effects: a Computational Study. *J. Phys. Chem. Lett.* **2012**, *3*, 2221–2227.
- Jing, Y.; Zhou, Z.; Cabrera, C. R.; Chen, Z. Metallic VS₂ Monolayer: A Promising 2D Anode Material for Lithium Ion Batteries. *J. Phys. Chem. C* **2013**, *117*, 25409–25413.
- David, L.; Bhandavat, R.; Singh, G. MoS₂/Graphene Composite Paper for Sodium-Ion Battery Electrodes. *ACS Nano* **2014**, *8*, 1759–1770.
- Naguib, M.; Kurtoglu, M.; Presser, V.; Lu, J.; Niu, J.; Heon, M.; Hultman, L.; Gogotsi, Y.; Barsoum, M. W. Two-Dimensional Nanocrystals Produced by Exfoliation of Ti₃AlC₂. *Adv. Mater.* **2011**, *23*, 4248–4253.
- Naguib, M.; Mashtalir, O.; Carle, J.; Presser, V.; Lu, J.; Hultman, L.; Gogotsi, Y.; Barsoum, M. W. Two-dimensional Transition Metal Carbides. *ACS Nano* **2012**, *6*, 1322–1331.
- Chang, F.; Li, C.; Yang, J.; Tang, H.; Xue, M. Synthesis of a New Graphene-Like Transition Metal Carbide by De-Intercalating Ti₃AlC₂. *Mater. Lett.* **2013**, *109*, 295–298.
- Yashin, A.; Ivanovskii, A. Atomic Structure, Comparative Stability and Electronic Properties of Hydroxylated Ti₂C and Ti₃C₂ Nanotubes. *Comp. Theor. Chem.* **2012**, *989*, 27–32.
- Hu, Q.; Sun, D.; Wu, Q.; Wang, H.; Wang, L.; Liu, B.; Zhou, A.; He, J. MXene: A New Family of Promising Hydrogen Storage Medium. *J. Phys. Chem. A* **2013**, *117*, 14253–14260.
- Khazaei, M.; Arai, M.; Sasaki, T.; Chung, C.-Y.; Venkataraman, N. S.; Estili, M.; Sakka, Y.; Kawazoe, Y. Novel Electronic and Magnetic Properties of Two-Dimensional Transition Metal Carbides and Nitrides. *Adv. Funct. Mater.* **2013**, *23*, 2185–2192.

41. Mashtalir, O.; Naguib, M.; Mochalin, V. N.; DallAgnese, Y.; Heon, M.; Barsoum, M. W.; Gogotsi, Y. Intercalation and Delamination of Layered Carbides and Carbonitrides. *Nat. Commun.* **2013**, *4*, 1716.
42. Lukatskaya, M. R.; Mashtalir, O.; Ren, C. E.; DallAgnese, Y.; Rozier, P.; Taberna, P. L.; Naguib, M.; Simon, P.; Barsoum, M. W.; Gogotsi, Y. Cation Intercalation and High Volumetric Capacitance of Two-Dimensional Titanium Carbide. *Science* **2013**, *341*, 1502–1505.
43. Tang, Q.; Zhou, Z.; Shen, P. Are MXenes Promising Anode Materials for Li Ion Batteries? Computational Studies on Electronic Properties and Li Storage Capability of Ti_3C_2 and $\text{Ti}_3\text{C}_2\text{X}_2$ (X = F, OH) Monolayer. *J. Am. Chem. Soc.* **2012**, *134*, 16909–16916.
44. Xie, Y.; Naguib, M.; Mochalin, V. N.; Barsoum, M. W.; Gogotsi, Y.; Yu, X.; Nam, K.-W.; Yang, X.-Q.; Kolesnikov, A. I.; Kent, P. R. Role of Surface Structure on Li-ion Energy Storage Capacity of Two-dimensional Transition Metal Carbides. *J. Am. Chem. Soc.* **2014**, *136*, 6385–6394.
45. Come, J.; Naguib, M.; Rozier, P.; Barsoum, M.; Gogotsi, Y.; Taberna, P.-L.; Morcrette, M.; Simon, P. A Non-Aqueous Asymmetric Cell with a Ti_3C -Based Two-Dimensional Negative Electrode. *J. Electrochem. Soc.* **2012**, *159*, A1368–A1373.
46. Er, D.; Li, J.; Naguib, M.; Gogotsi, Y.; Shenoy, V. B. Ti_3C_2 MXene as a High Capacity Electrode Material for Metal (Li, Na, K, Ca)-ion Batteries. *ACS Appl. Mater. Interfaces* **2014**, *6*, 11173–11179.
47. Peng, Q.; Guo, J.; Zhang, Q.; Xiang, J.; Liu, B.; Zhou, A.; Liu, R.; Tian, Y. Unique Lead Adsorption Behavior of Activated Hydroxyl Group in Two-Dimensional Titanium Carbide. *J. Am. Chem. Soc.* **2014**, *136*, 4113–4116.
48. Kim, Y.; Park, Y.; Choi, A.; Choi, N.-S.; Kim, J.; Lee, J.; Ryu, J. H.; Oh, S. M.; Lee, K. T. An Amorphous Red Phosphorus/Carbon Composite as a Promising Anode Material for Sodium Ion Batteries. *Adv. Mater.* **2013**, *25*, 3045–3049.
49. Datta, D.; Li, J.; Shenoy, V. B. Defective Graphene as a High-Capacity Anode Material for Na- and Ca-Ion Batteries. *ACS Appl. Mater. Interfaces* **2014**, *6*, 1788–1795.
50. Muldoon, J.; Bucur, C. B.; Oliver, A. G.; Sugimoto, T.; Matsui, M.; Kim, H. S.; Allred, G. D.; Zajicek, J.; Kotani, Y. Electrolyte Roadblocks to a Magnesium Rechargeable Battery. *Energy Environ. Sci.* **2012**, *5*, 5941–5950.
51. Lu, Z.; Schechter, A.; Moshkovich, M.; Aurbach, D. On the Electrochemical Behavior of Magnesium Electrodes in Polar Aprotic Electrolyte Solutions. *J. Electroanal. Chem.* **1999**, *466*, 203–217.
52. Gregory, T. D.; Hoffman, R. J.; Winterton, R. C. Nonaqueous Electrochemistry of Magnesium Applications to Energy Storage. *J. Electrochem. Soc.* **1990**, *137*, 775–780.
53. Do, G. X.; Paul, B. J.; Mathew, V.; Kim, J. Nanostructured Iron (iii) Oxyhydroxide/(vi) Oxide Composite as a Reversible Li, Na and K-Ion Insertion Electrode for Energy Storage Devices. *J. Mater. Chem. A* **2013**, *1*, 7185–7190.
54. Liu, Y.; Fan, F.; Wang, J.; Liu, Y.; Chen, H.; Jungjohann, K. L.; Xu, Y.; Zhu, Y.; Bigio, D.; Zhu, T.; *et al.* *In Situ* Transmission Electron Microscopy Study of Electrochemical Sodiation and Potassiation of Carbon Nanofibers. *Nano Lett.* **2014**, *14*, 3445–3452.
55. Buldum, A.; Tetiker, G. First-Principles Study of Graphene-Lithium Structures for Battery Applications. *J. Appl. Phys.* **2013**, *113*, 154312.
56. Poizot, P.; Laruelle, S.; Grugeon, S.; Dupont, L.; Tarascon, J. Nano-Sized Transition-Metal Oxides as Negative-Electrode Materials for Lithium-Ion Batteries. *Nature* **2000**, *407*, 496–499.
57. Chiku, M.; Takeda, H.; Yamaguchi, Y.; Higuchi, E.; Inoue, H. Study on the Electrolyte Containing AlBr_3 and KBr for Rechargeable Aluminum Batteries. *Int. J. Chem.* **2013**, *5*, 1–8.
58. Kohn, W.; Sham, L. J. Self-Consistent Equations Including Exchange and Correlation Effects. *Phys. Rev.* **1965**, *140*, A1133.
59. Blöchl, P. E. Projector Augmented-Wave Method. *Phys. Rev. B* **1994**, *50*, 17953.
60. Kresse, G.; Furthmüller, J. Efficient Iterative Schemes for *Ab Initio* Total-Energy Calculations using a Plane-Wave Basis Set. *Phys. Rev. B* **1996**, *54*, 11169.
61. Perdew, J. P.; Burke, K.; Ernzerhof, M. Generalized Gradient Approximation Made Simple. *Phys. Rev. Lett.* **1996**, *77*, 3865.
62. Klimeš, J.; Bowler, D. R.; Michaelides, A. Van der Waals Density Functionals Applied to Solids. *Phys. Rev. B* **2011**, *83*, 195131.
63. Monkhorst, H. J.; Pack, J. D. Special Points for Brillouin-Zone Integrations. *Phys. Rev. B* **1976**, *13*, 5188–5192.
64. Henkelman, G.; Uberuaga, B. P.; Jónsson, H. A Climbing Image Nudged Elastic Band Method for Finding Saddle Points and Minimum Energy Paths. *J. Chem. Phys.* **2000**, *113*, 9901–9904.
65. Vinet, P.; Rose, J. H.; Ferrante, J.; Smith, J. R. Universal Features of the Equation of State of Solids. *J. Phys.: Condens. Matter* **1989**, *1*, 1941.
66. Baroni, S.; de Gironcoli, S.; Dal Corso, A.; Giannozzi, P. Phonons and Related Crystal Properties from Density-Functional Perturbation Theory. *Rev. Mod. Phys.* **2001**, *73*, 515.
67. Togo, A.; Oba, F.; Tanaka, I. First-Principles Calculations of the Ferroelastic Transition Between Rutile-Type and CaCl_2 -Type SiO_2 at High Pressures. *Phys. Rev. B* **2008**, *78*, 134106.